**Periodica Polytechnica Chemical Engineering**, 68(3), pp. 326–337, 2024

# The Nanostructure Based SnS Chalcogenide Semiconductor: A Detailed Investigation of Physical and Electrical Properties

Mostefa Benhaliliba[1*], Abbas Ayeshamariam[2], Yusuf Selim Ocak[3,4]

[1] Film Device Fabrication-Characterization and Application FDFCA Research Group USTOMB, 31130 Oran, Algeria
[2] Department of Physics, Khadir Mohideen College, 614701 Adirampattinam, Thanjavur District, Tamil Nadu, India
[3] Institute of Nanotechnology, Jordan University of Science and Technology, P. O. B. 3030, 22110 Irbid, Jordan
[4] Smart-Lab, Dicle University, 21280 Diyarbakir, Türkiye
[*] Corresponding author, e-mail: mostefa.benhaliliba@univ-usto.dz

Received: 08 March 2024, Accepted: 17 June 2024, Published online: 25 July 2024

**Abstract**

In this research, we fabricate SnS films using a low-cost spray pyrolysis technique. Several parameters such as grain size, textural coefficient, Sn concentration, root mean square (RMS), optical band gap, Urbach and dispersion energy are determined by the mean of X-ray diffraction pattern, UV-Vis measurements, surface morphology observation by scanning electron microscopy (SEM)-energy dispersive X-ray spectroscopy (EDX), transmission electron microscopy (TEM), selective area electron diffraction (SAED) and atomic force microscopy (AFM). Furthermore, SnS thin films exhibit a polycrystalline structure having a low grain size of 6.1 nm along principal (111) orientation. The optical band gap is around 1.9 eV and Urbach energy is of 740 meV. The dielectric parameters of chalcogenide SnS thin film are varying with photon energy within ultraviolet-visible-infrared (Uv-Vis-IR) bands. Besides, the single oscillator $E_0$ and $E_d$ energies are found to be 2.03 and 3.28 eV, respectively, using the Wemple and DiDomenico (WDD) model.

Electrical measurements of SnS thin films deposited onto Indium Tin Oxide (ITO) substrate are accomplished and current-voltage (*I*–*V*) characteristics of $SnO_2$/SnS/ITO, are shaped in dark and room temperature conditions. Photovoltaic parameters like open circuit voltage ($V_{oc}$), short circuit current ($I_{sc}$), fill factor (*FF*) and power conversion efficiency ($\eta$) values are determined and $SnO_2$/SnS/ITO junction records the highest values.

**Keywords**

SnS chalcogenide thin film, spray pyrolysis, X-ray analysis, transmittance, nanostructures, junction

## 1 Introduction

Due to their outstanding characteristics and important potential for application in optoelectronic devices, binary compounds based on the Sn-S system have received a lot of research over the past few decades. Tin sulfide SnS is a chalcogenide, ABX (X = S, SeTe), semiconductor having a place with the IV–VI family. It is perhaps the main oxide semiconductors described by the double nature *p* and *n* conductivity relying upon the tin concentration, which permits the production of homojunctions. A few micron thick film having a large absorption coefficient (> $10^5$ $cm^{-1}$) [1–2], e.g., can absorb all photons with energies noteworthy higher than its gap energy comparing with CdTe and PbS chalcogenide semiconductors. The SnS is direct and indirect semiconductor whose gap is ranging within (1.1–1.43 eV) [3]. Due to their electro-optical, environmental safety, and cost characteristics – all of which are crucial for photovoltaic applications – tin sulfide semiconductor materials ($SnS_x$) rank among the most thoroughly investigated photovoltaic semiconductor [4]. The *p*- and *n*-type SnS thin films via vacuum-free growth process are already fabricated as reported by Mohan et al. [1]. SnS thin films are grown on glass substrates using several processes as radio-frequency (RF) magnetron sputtering [5], thermal evaporation [6], spray pyrolysis (SP) [7, 8], successive ionic layer adsorption and reaction (SILAR) method at high solution temperature [9], hydrothermal technique [10] and vacuum-free growth [11]. Tin monosulfide (SnS), a suitable IV–VI semiconductor 2D material, is being investigated for potential applications such as photocathode solar cells and a photoelectrochemical (PEC) water splitting due to its good visible absorption, fast separation efficiency caused by high carrier mobility, non-toxic abundant earth constituent elements, and high

**Cite this article as:** Benhaliliba, M., Ayeshamariam, A., Ocak, Y. S. "The Nanostructure Based SnS Chalcogenide Semiconductor: A Detailed Investigation of Physical and Electrical Properties", Periodica Polytechnica Chemical Engineering, 68(3), pp. 326–337, 2024. https://doi.org/10.3311/PPch.36830

chemical and environmental stability. A *p*-type conductivity SnS semiconductor has a suitable band gap of 1.7–2.1 eV [12]. The use of RF sputtering for making SnS/Ag/SnS films for photovoltaic applications is previously mentioned in literature [13]. In this research, we fabricated SnS based thin film and *p-n* junction diode using a low-cost spray pyrolysis technique onto glass and Indium Tin Oxide (ITO) substrates. Up to our knowledge, many researches have been reported on SnS thin films but no papers have reported on SnS based thin films and $SnO_2$/SnS *pn* junctions and their physical-electrical properties.

## 2 Experimental procedure

The glass substrate is carefully cleaned with chromic acid and doubly distilled water. Firstly, ITO of resistivity 2–5-Ω × cm is thoroughly cleaned by agitating in trichloroethylene (TCE) and acetone, with an intermittent cleaning by deionized and doubly distilled water. Later they are cleaned with acetone in order to remove the residual oxide. After drying, the substrates are transferred to the substrate holder for thin film deposition.

SnS, $SnO_2$ in SnS/$SnO_2$ thin films are prepared in the indigenously built chemical spray pyrolysis setup. SnS thin films are produced with SP technique onto glass substrate at 350 °C with 5 mL/min for 10 min. SnS chalcogenide film is produced from 0.08 M of $SnCl_2 \cdot 2H_2O$ and $Na_2S$ dissolved in isopropyl alcohol. The parameters such as the substrate-nozzle distance (SND) and the flow rate of the solution are kept constant at 24 cm and 5 mL/min, respectively. The solution and its pressure are kept constant at 0.7 kg/cm$^2$ for all depositions. The baked films are removed from the spray chamber after 4 h, after they cooled to room temperature and are stored in a moist free environment. The thickness of thin films evaluated with gravimetric method and surface profiler are in the range 0.4–0.5 μm. Electrical contacts are made between the film surface and the holder with carbon tape to avoid charging. For the $Sn_2O$/SnS junction, the solution is made with 0.40 M of $SnCl_4 \times 5H_2O$ and 0.025 M of SnS as precursors dissolved in 100 mL of ethyl alcohol. 5 mL of 0.1 M of HCl was added to the solution as a catalyst in order to increase the solubility and to facilitate the simultaneous condensation and elimination reactions. The X-ray diffraction analysis is carried out at room temperature with an automatic X-ray diffraction BRUKER-AXS type D2 diffractometer using the $Cu_{K\alpha}$ ($\lambda$ = 1.5405 Å) wavelength in the 2$\theta$ 10–80° range at room temperature by a step of 0.02 at 40 kV. The optical transmittance and reflectance are measured using a Shimadzu UV-3600 spectrophotometer. Surface morphology is characterised using a scanning electron microscope (SEM) from Hitachi S-3400N, Japan. The 2D atomic force microscope (AFM) images are obtained in contact mode. The junction characteristics in the dark and clearly A (GE-ELH) lamp is used as light source. This lamp has a power of 300 W and runs on 120 V. It also has a reflector to produce a bright white light on the surface of the solar cell. The spectral distribution of this lamp is nearly identical to the solar spectrum, with the majority of the luminous intensity distributed in the visible range (400 to 700 nm). This intensity is measured with a Suryamapi intensity meter in mW/cm$^2$. The values *I* and *V* are measured using PHILIPS n°341 digital multimeters. The *I–V* characteristics in dark condition are measured by completely enclosing the solar cell in a black box and polarizing it with Aplab d.c. alimentation ranging from +2.0 V to –2.0 V.

## 3 Exploitation and discussion of results

### 3.1 SnS thin film

#### 3.1.1 X-ray diffraction

Based upon X-ray diffraction analysis, our samples present a polycrystalline structure according to preferential (111), (200) and (311) orientation as seen in Fig. 1, showing intense peaks at 28.06º, 35.34° and 53.05° as tabulated in Table 1. According to literature, the main intense peaks of SnS films prepared by SILAR technique, are (111), (201) and (220) [14]. Others less intense are (311), (222), (400), (331), (420) and (422) [14]. As indicated in Table 1 and according to $\Delta\theta$ values, three main peaks are shifted to lower 2$\theta$ angle unlike (200) which is shifted to higher ones. This fact confirms the polycrystalline structure of SnS chalcogenide based thin film. As shown in the X-ray

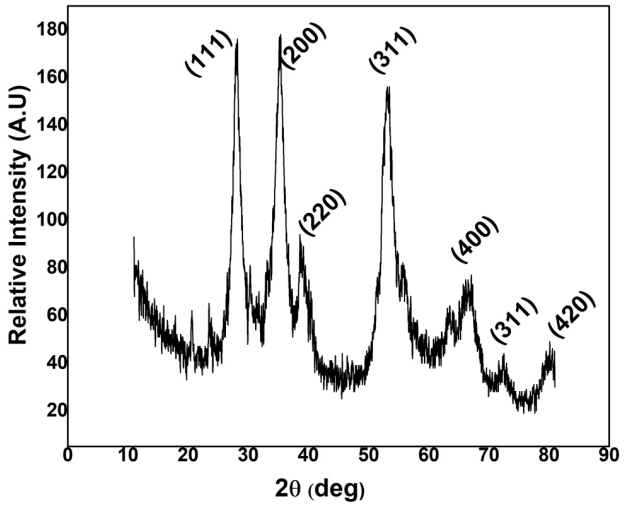


**Fig. 1** X-ray diffractogram of SnS thin films prepared by spray pyrolysis

**Table 1** Structural parameters of SnS film*

| Orientations (*hkl*) | 2$\theta$ (°) | $\Delta\theta$ (°) | Intensity of peak | $\beta$ (°) | Peak area | *G* (nm) | *Tc* | $\delta$ (×10$^{15}$) (1/m$^2$) | $\varepsilon$ (%) |
|---|---|---|---|---|---|---|---|---|---|
| (111) | 28.06 | –0.31 | 175 | 1.40 | 155.21 | 6.10 | 1.02 | 27 | 0.024 |
| (200) | 35.34 | 2.19 | 176 | 1.51 | 151.5 | 5.84 | 1.05 | 29 | 0.021 |
| (311) | 53.05 | –2.95 | 154 | 1.68 | 149.5 | 5.52 | 0.91 | 33 | 0.015 |
| (400) | 66.61 | –2.32 | 75 | - | - | - | - | - | - |

* 2$\theta$ (°) is Bragg angle, $\Delta\theta = \theta$measured-$\theta$standard, $\beta$ is full width at half height, *G* is grain size, *Tc* is the textural coefficient, $\delta$ is the dislocation number and $\varepsilon$ is the residual strain

pattern, a (111)-oriented cubic crystal structure is revealed with a space group $F\bar{4}3m$(216), $a$ = 5.445 Å [15].

The relation between the inter-planar distance $d$, the lattice parameter $a$, and the Miller indices ($h$,$k$,$l$) is given by [16],

$$\frac{1}{d^2} = \left( \frac{h^2 + k^2 + l^2}{a^2} \right). \tag{1}$$

$\Delta\theta$ is the difference between the measured value of $\theta$ (where 2$\theta$ is from X-ray analysis), and its value given by standard JCDPS card. $G$ is the grain size given by Eq. 5 for the main peak by using a gaussian fit parameters. $\delta$ is expressed in Eq. 4, $\varepsilon$ is expressed in Eq. 3. and $T_c$ is given by Eq. 2. Table 1 lists the structural parameters of SnS chalcogenide material based thin film. Grain size is found to be within 5.52–6.10 nm. Such findings are nanoscaled as confirmed by SEM, AFM, TEM microscopic observations. The textural coefficient of SnS film is ranged within 0.9–1.05. This fact confirms the good crystallinity of SnS film for the high value of $T_c$. The dislocation number is ranging between 27 × 10$^{15}$ and 33 × 10$^{15}$ 1/m$^2$, residual strain varying 0.015–0.024 are the obtained values of SnS film from X-ray pattern analysis. It is reported that SnS orthorhombic exhibits the lattice parameters $a$ = 11.20 Å, $b$ = 3.99 Å and $c$ = 4.34 Å, $p$-type semiconductor is revealed [17].

Based upon the X-ray pattern, the intense orientations of cubic SnS are located at 2$\theta$ 26.58, 30.77 and 31.68, and less intense at 35.47, 39.47, 44.13, 48.38, 50.37 and 57.07. The resulting peaks have a good match with the cubic SnS diffraction peaks with lattice constant a of 11.6 Å that have been described previously [18–19]. The (111), (131), (141), (112) and (122) orientations of orthorhombic SnS phase are located at 31.5°, 39.0°, 44.8°, 51.1°and 53.1º are reported as cited by Olgar et al. [5].

It is reported that orthorhombic SnS phase demonstrated a polycrystalline structure recording (201), (011), (111) and (400) planes situated respectively at 26.45°, 30.69°, 31.60° and 32.15° as Nouri et al. cited before [7].

The textural coefficient ($T_c$) is considered to define the preferential orientation (*hkl*) using the following relation [20],

$$T_c = \frac{I_{(hkl)} / I_{0(hkl)}}{\frac{1}{N}\sum I_{(hkl)} / I_{0(hkl)}}. \tag{2}$$

Where $I_{(hkl)}$ is the measured intensity of the plane (*hkl*), $I_{0(hkl)}$ is the standard intensity according to cubic SnS 77–3356 JCPDS card while orthorhombic SnS structure obeys to card No: 01-071-3679 [7] and $N$ is a reflection number. Residual stress ($\varepsilon$) expresses as follows [21],

$$\varepsilon = \frac{\beta}{4\tan\theta}. \tag{3}$$

$\beta$ is the full width at half height of the intensity peak, and 2$\theta$ is Bragg angle.

Dislocation density $\delta$, as a function of grain size $G$, is given by [21],

$$\delta = \frac{1}{G^2}, \tag{4}$$

where $G$ is the grain size given by Eq. 5.

It is confirmed that grain size of SnS film is increasing from 14.01 nm for (002) orientation to 88.18 nm for (103) orientation while strain value is insignificant for (103) direction. These results reveal as well as the X-ray pattern reveal the high crystalline quality of the film. Structural data of SnS film extracted from X-ray analysis are gathered in Table 1. The grain size of SnS chalcogenide material based thin film, $G$, is calculated using Scherrer formula as [21],

$$G = \frac{0.94\lambda}{\beta\cos\theta}. \tag{5}$$

Where $\lambda$ is the X-ray wavelength used (1.54 Å). Grain size values 8–20 nm of SnS prepared by sputtering are found as reported by Olgar [5]. As reported in previous works, SnS thin films in cubic SnS and orthorhombic $SnS_2$,

and $Sn_2S_3$ are produced and others phases like cubic SnS and orthorhombic $SnS_2$, $Sn_2S_3$ are obtained as cited in reports [18]. cited in reports [18]. Such phases are formed in *Pnma*, $F\bar{4}3m$, $P\bar{3}m$ space groups and cubic crystalline structure exhibits a lattice parameter of 6.5 Å [22].

### 3.2 Textural analysis of SnS based thin film

#### 3.2.1 SEM and EXD analysis

The surface morphology of SnS film is observed by SEM as seen in Fig. 2a. The profile of SnS film shows a homogeneous, compact and dense aspect. Nanograins look like sheets are displayed in surface. This result is in good agreement with that obtained by X-ray pattern. Quasi-spherical forms are present in surface as shown by arrows. The chemical composition of SnS thin films and its statistical data of Sn and S atoms are given by EDX study as illustrated in Fig. 2b. Sn and S are two elements analyzed by EDX with different intensities with high amount of Sn. EDX obtained values are gathered in Table 2. Similar tendency is already reported for orthorhombic phase of SnS crystal because S atom is more volatile than Sn atom. This finding corroborates with previous results of orthorhombic SnS [23–24]. This research also demonstrates that our SnS film is composed entirely of tin and sulfur, and that the glass substrate has no effect on the film. Curved lines and grains looking like dots are observed in SEM picture of SnS film as shown by arrows in Fig. 2a. The surface is homogeneous with a few voids. Grain tangling is seen on the surface, giving the film a compacted aspect. As it has already reported, the nanoflakes shaped like grains of SnS with pinholes and a crack-free surface are presented [19]. EDX diagram shows 56 atom% for Sn and 13 atom% for S recording a S/Sn ratio less than ¼ as sketched in the inset of Fig. 2b.

Although the SEM pictures of as-deposited and annealed SnS thin films indicated low crystallinity, the thin film displayed greater grain size. This outcome is consistent with the film results given by X-ray diffractogram and Raman spectroscopy [5].

In the SEM micrographs needle-shaped grain morphology was discovered in sprayed SnS film as cited by Jeganath [8]. Using vapor phase deposition technique, platelet crystals of SnS thin films are produced as confirmed by SEM images [25].

The SnS film surface morphology at various substrate temperatures are already studied. Grains look like rice as seen by SEM analysis. Rice grains are distributed nearly uniformly on the surface of the SnS film, with a few holes that can alter in size. Sn and S cations are found to be 50 and 49.9% as revealed by EDX analysis [26].

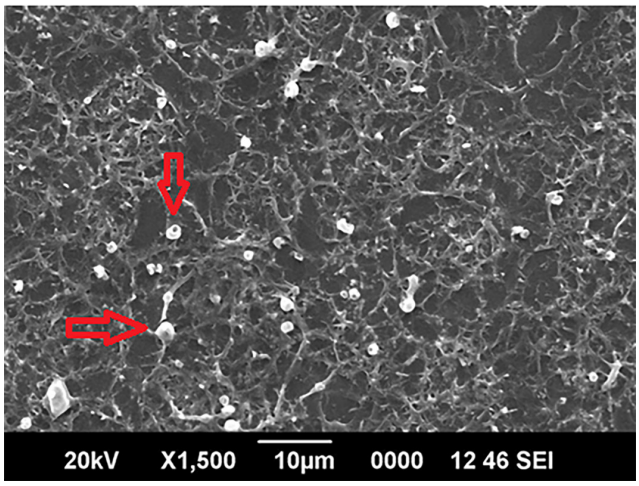


**Fig. 2** Scanning electron microscope images, arrows show nanograins

**Table 2** Data obtained from EDX

| Element | Net counts | Weight (%) | Atom (%) |
|---|---|---|---|
| Sn | 2837 | 18.66 | 56.09 |
| S | 17782 | 7.75 | 13.28 |
| Sn | 87124 | 60.17 | 25.20 |
| S | 18176 | 13.42 | 5.43 |
| Total | | 100.00 | 100.00 |

#### 3.2.2 2D and 3D-AFM scanned images

Fig. 3 A–C display the 2D histogram and 3D AFM pictures of SnS films produced onto glass. The analyzed (2µm × 2µm) surface reveals the uniform distribution of grains, compact with micro-crystallites which confirm the presence of sheets.

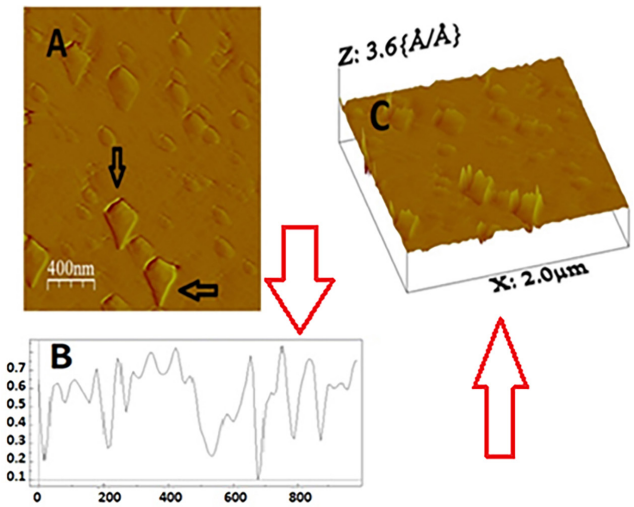


**Fig. 3** 2D (A), histogram (B), and 3D-scanned AFM (C) (2µm × 2µm) picture of SnS film. Arrows show the nanograins (A)

This result supports that demonstrated by SEM analysis. The root mean square (RMS) given by the horizontal cross section at 1000 nm is ranging in 0.1–0.7 µm as depicted in Fig. 3B. As reported in previous works, AFM images confirm that grain growth is dependent on film thickness for $\pi$-SnS films grown by varying the number of deposition cycles using chemical bath deposition [27]. Moreover, the grain boundaries become more visible as both film thickness and grain size increase. The occurrence of larger grains as film thickness increases could be attributed to the coalescence or agglomeration of smaller grains during a chemical bath deposition (CBD) growth [27]. Effect of molar concentration on triethanolamine (TEA) added SnS thin films grown by SILAR route is investigated. Surface roughness and surface height are found to be 0.16–0.93 nm and 0.44–3.72 nm, respectively for an electron microscope magnification of 10 and 5 µm as mentioned by Mani et al. The particle height ranges from 0.44 to 1.27 nm, and the particle size is irregular. The smoothness improves as the maximum particle height decreases [28].

### 3.2.3 TEM and SAED analysis

High resolution TEM image of SnS film is accomplished at 20 nm scale as displayed in Fig. 4A, while Fig. 4B displays the selected area electron diffraction (SAED) images of the as-grown sample showing halo rings. The five circles of the layered SnS structure correspond to the (111), (200), (220), (311), (400) intense peaks in the X-ray diffractogram. SAED images, hence, confirm improved ordering or crystallinity with increasing grain size, explaining the trend in electron diffraction with grain size. Both sample types showed a thick and consistent surface microstructure, as was already indicated.

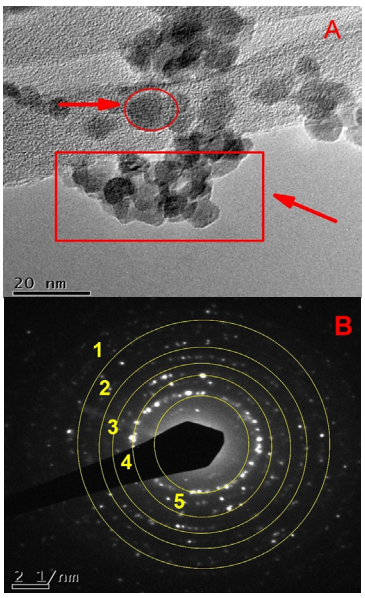


**Fig. 4** High resolution TEM image of SnS film. 20 nm scale is displayed at bottom, Nano-aggregates are displayed by arrows (A). Selective area electron diffraction SAED (B). 2 1/ nm scale is displayed at bottom. Circles 5, 4, 3, 2 and 1 correspond respectively to (111), (200), (220), (311), (400) directions extracted from X-ray diffractogram.

It is observed from the TEM image that the average size of these particles is approximately 10 nm. So, grains look like semicircular and circular forms as indicated by open circle and rectangle and arrow in Fig. 4A.

The film surface shows two different contrasts neighboring each other. Assembled circular objects confirm cubic SnS phase occurrence and dispersed ones might correspond to the other SnS phase in being present very small amount. In the SAED analysis of SnS film the rings 1–5 are related to the intensive peaks. Analyzed by TEM microscope, the $\alpha$-SnS phase is dominant in the sample, a small amount of $\pi$-SnS is also detected [29]. Several planes corresponding to *p*-SnS are observed by SAED analysis as cited by Rodríguez-Guadarrama et al. [30]. In this work (400), (410), and (222) orientations are identified by TEM analysis. According to SAED, the *p*-SnS (221), (222), (400), (410), (421), and (440) planes are the primary diffraction spots, which are in agreement with the X-ray diffractogram [30].

### 3.3 UV-Vis-IR measurements

The transmittance *T* and reflectance *R* versus photon wavelength $\lambda$ within the UV-Vis-IR range of sprayed SnS thin film at 350 °C are depicted in double Y-axis in Fig. 5. A drastic increase of transmittance profile from UV is observed with the highest point of 73.7% at 1093 nm. The transmittance shows a slight peak of 13.7% in the UV range whereas *R* a decay in UV and reaches roughly a plateau from 600 to 1100 nm. Transmittance in terms of absorption coefficient $\alpha$ and film thickness *e* is expressed by the Beer-Lambert law [31],

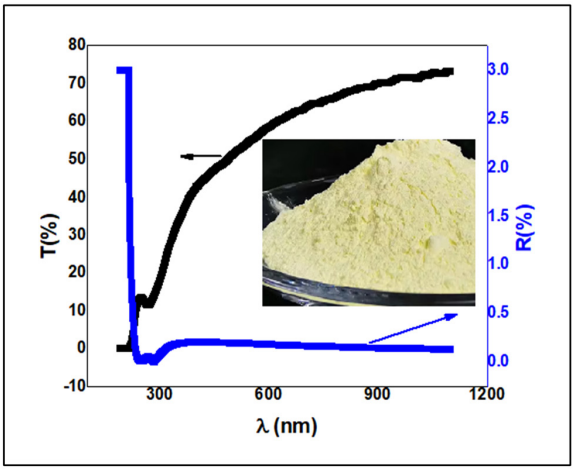


**Fig. 5** The transmittance (left) and reflectance (right) versus photon wavelength of SnS thin film produced by spray pyrolysis route. Inset shows SnS raw material

$$T = (1-R)^2 \, e^{-ae} \cdot \tag{6}$$

Where $R$ is the reflectance coefficient and $\alpha$ depends on $e$ and $T$ as follows [32],

$$\alpha = \frac{1}{e} \ln\left(\frac{100}{T}\right). \tag{7}$$

It is noted that the films are highly transparent in the visible region and poorly in the ultraviolet region. The transmittance profile does not exhibit oscillations. Similar growth in transmittance $T$–ln$\lambda$ curve was found by Kafashan et al. [33]. Orthorhombic SnS presented a band gap of 1.09 eV and 1.32 eV for indirect and direct transition semiconductors [34].

Such features open to our device, having $\pi$-cubic crystal structure, many applications such as optical window in solar cell. Such optical properties could be interpreted by the high crystalline structure and the morphology of films due to their increase in grain size. Because the number of photons absorbed by the materials rose as the crystallinity and thickness of the SnS thin films grew due to the growing pressure, the transmittance spectrum shifted to the long infrared wavelengths. Highest values of transmittance are recorded in the 1200–2000 nm region and the band gap $E_g$ is ranged within 1.47–1.56 eV as written before [35].

Fig. 6 demonstrates the profile of absorbance $A$ in the 200–1100 nm range. A strong absorbance of our film within $\lambda < 300$ nm, which defines the near band edge in UV, is clearly observed. So, a transition inter-band may cause this strong absorbance which explains its use for optical bandgap determination. Consequently, the SnS material is transparent in such high wavelength bands.

The gap energy of SnS film is calculated by theoretically adjusting the above cited curve of $(\alpha h\nu)^{0.5}$ [35] as a function of the input photon energy $h\nu$ as displayed in Fig. 7. The estimated bandgap is 1.9 eV for SnS film. Due to its high optical absorption coefficient (higher than 104 cm$^{-1}$) tin sulfide has attracted the most interest among various semiconducting metal chalcogenides [2]. The SnS thin film displays the best gap energy 1.52 eV as Nouri reported [7].

Urbach energy $E_u$ is determined by plotting ln$\alpha$ against energy $h\nu$ according to the following equation [6],

$$E_u = \frac{dh\nu}{d\ln\alpha}. \tag{8}$$

The Urbach energy $E_u$ (meV) can be obtained by plotting the linear component of the ln$\alpha$ vs. $h\nu$ curve as shown in Fig. 8. $E_u$ value is found using the slope of the linear component of ln$\alpha$ vs. $h\nu$ value as indicated by Eq. 8, within 1–6 eV energy range. From curve ln$\alpha$–$h\nu$, slope is found to be 1.35 as

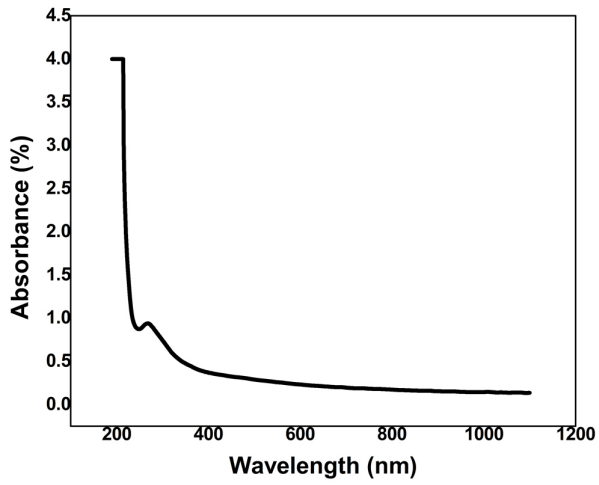


**Fig. 6** Absorbance profile vs. photon wavelength of as-grown SnS films

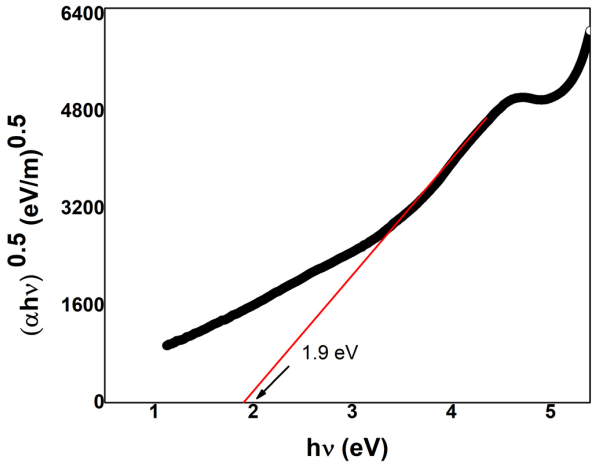


**Fig. 7** Plotting of $(\alpha h\nu)^{0.5}$ vs. photon energy of as-grown SnS films. Inset indicates the straightline to $\nu$ axis evaluating the optical bandgap

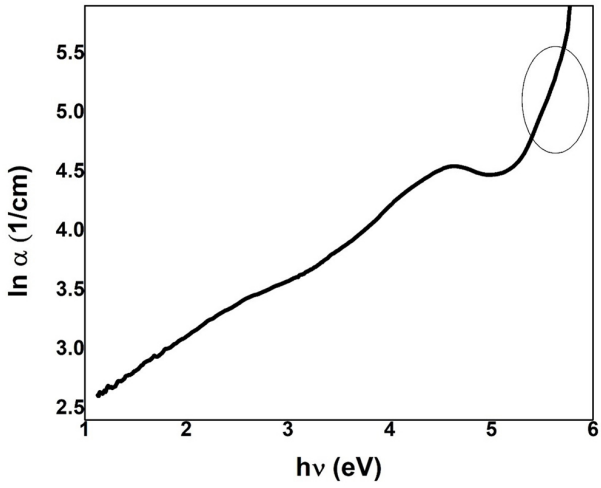


**Fig. 8** Plotting of $\alpha$ as a function of photon energy $h\nu$ of SnS thin film (disorder determination). Linear part of curve is indicated by open circle

indicated by the open circle in Fig. 8 and $E_u$ = 740 meV. $E_u$ is much less than, and the ratio of $E_u$ to $E_g$ is approximately $E_u/E_g \sim 0.4$. This minor value is due to a decrease of defects and an increase of grain size which explains the drop of disorder inside the SnS crystalline structure. SnS, one of the few inherent *p*-type semiconductor materials, has drawn a lot of attentions due to its exceptional and distinctive characteristics of high conductivity and enormous absorption coefficient (> 104 $cm^{-1}$) [10]. The orthorhombic SnS crystal structure is deformed like the structure of sodium chloride. The direct and indirect bandgaps for SnS are found to be 1.32 eV and 1–1.3 eV, respectively [10]. Cu-doped SnS thin film present an optical band gap ranging from 1.83 to 1.90 eV. All films reveal high electrical resistivity ($10^4$–$10^5$ Ω cm), low hole concentration ($10^{11}$–$10^{12}$ $cm^{-3}$), and *p*-type conductivity, according to Hall-effect experiments as mentioned earlier [10]. A transmittance of sprayed SnS film reaches 55% at 1400 nm as Sarica reported [36].

A bandgap within 1.84–1.45 eV is confirmed by SnS film produced by chemical spray pyrolysis (CSP) technique and a highest optical absorption coefficient of $10^5$ $cm^{-1}$ in the visible band is recorded [1, 37].

### 3.4 Dielectric parameters and single oscillator model

According to the theory the electron oscillation excitation between the conduction and valence bands (inter-band transitions in and around the band edge) is responsible for the refractive index of the materials in the visible range. In order to explore the dielectric behavior of chalcogenide SnS based thin film, the extinction coefficient $k\lambda$, and refractive index are plotted as a function of photon wavelength $\lambda$ using $R = 100–T–A$ and expressed as [38–40],

$$k(\lambda) = \frac{\lambda}{4\pi t} \ln\left[\left[\frac{(1-R(\lambda))^2}{2T(\lambda)}\right] + \sqrt{\left(\frac{(1-R(\lambda))^4}{4(T(\lambda))^2} + (R(\lambda))^2\right)}\right], \tag{9}$$

$$n(\lambda) = \left[\frac{(1+R(\lambda))}{1-R(\lambda)}\right] + \sqrt{\left(\frac{4R(\lambda)}{(1-R(\lambda))^2} - (k(\lambda))^2\right)}, \tag{10}$$

$$\alpha(\lambda) = \frac{1}{t} \ln\left\{\left[\frac{(1-R(\lambda))^2}{2T(\lambda)}\right] + \sqrt{\left(\frac{(1-4R(\lambda))}{(4T(\lambda))^2} - (R(\lambda))^2\right)}\right\}, \tag{11}$$

where $t$ is the layer thickness.

Fig. 9 depicts the variation of $k$ of SnS chalcogenide film versus the photon energy. It is noted that $k$ is decreasing from low photon energy to higher energy showing a minimum at 5.2 eV as seen in Fig. 9, while a Gaussian shape curve is found for the refractive index $n$ as dispkayed in Fig. 10. This curve reaches a maximum of 2.6 at 3.12 eV within visible range. Glass exhibits a value of 1.5, and for $SnS_2$ $n$ = 2.49–2.8 [39]. Lower values of $n$ 1.35–1.66 are reported before [5].

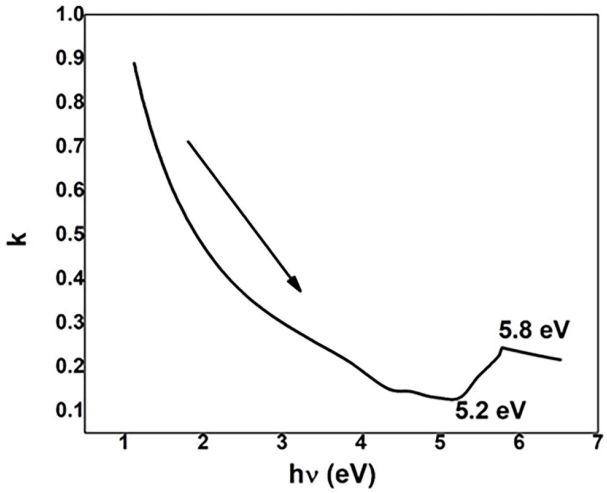


**Fig. 9** Extinction coefficient $k$ of SnS film vs. photon energy. Minimum of $k$ at 5.2 eV is marked

$R$ in terms of $n$ and $k$ is expressed as [40],

$$R = \frac{(n-1)^2 + k^2}{(n+1)^2 + k^2}, \tag{12}$$

$$k = \frac{\alpha\lambda}{4\pi}. \tag{13}$$

The expression is used to fit the refractive index in terms of the photon energy $h\nu$, the energy of the effective dispersion oscillator $E_0$, and the dispersion energy $E_d$. Wemple 's

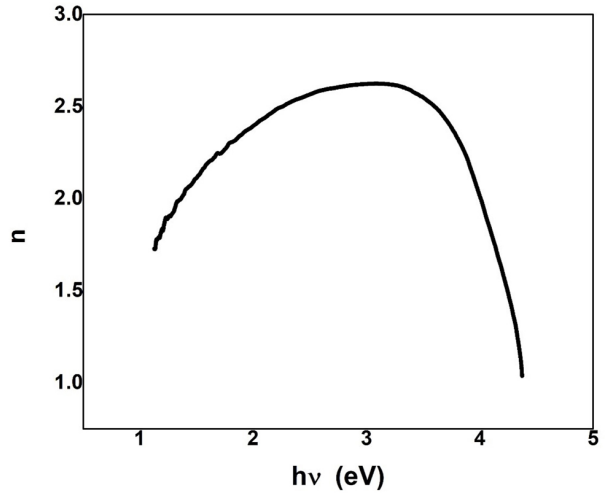


**Fig. 10** Refractive index $n$ of SnS film vs. photon energy. Max 2.62 is indicated

and DiDomenico's single oscillator model presents the following expression between $n$ and $hv$ [41–42],

$$\frac{1}{n^2-1}=\frac{E_0}{E_d}-\frac{(hv)^2}{E_0E_d}. \quad (14)$$

The ratio $E_0/E_d$ = 0.62 is the intercept and the slope $1/E_0E_d$ = 0.15. So, the obtained values are $E_d$ = 3.28 eV, $E_0$ = 2.03 eV from the linear fit of $1/(n^2–1)$ curve against $(hv)^2$ of SnS film within 1.8–2 eV² as indicated in Fig. 11. Compared to the optical band gap, the ratios $E_g/E_d$ 0.6 and $E_g/E_0$ 0.9 indicated the difference. Variation of the parameters $E_d$ and $E_0$ for the single oscillator model proposed by Wemple and DiDomenico vary with the grain size. While $E_d$ rises with increasing grain size, $E_0$ follows the same trend as the band-gap as reported earlier [43]. $E_0$ and $E_g$ = 1.2–2.6 eV and 1.8–2.2 eV, respectively, when grain size goes from 10 to 30 nm [43].

### 3.5 Photoelectrical properties of $SnO_2$/SnS junction

A schematic cross-section of the Ag/$SnO_2$/SnS/glass and Ag/$SnO_2$/SnS/ITO junction diodes is drawn as seen in Fig. 12. In aim to explore electrical behavior of devices, electrical characterizations of $SnO_2$/SnS/glass and $SnO_2$/SnS/ITO are achieved. Here, the electrical property evaluations of our devices based on $SnO_2$ and SnS are performed in the dark and at room temperature as shown in Fig. 13 (a, b). Such figures exhibit the transport mechanism of thin films from solar cells ($SnO_2$/SnS/glass and $SnO_2$/SnS/ITO) in dark, where the current increases as the bias voltage changes. We notice that the variation of current vs. voltage is nearly linear, indicating that the contacts of silver are ohmic. It is displayed roughly a curve growing from –1 µA to 1 µA within –0.3 V–0.3 V and –4 V–4 V

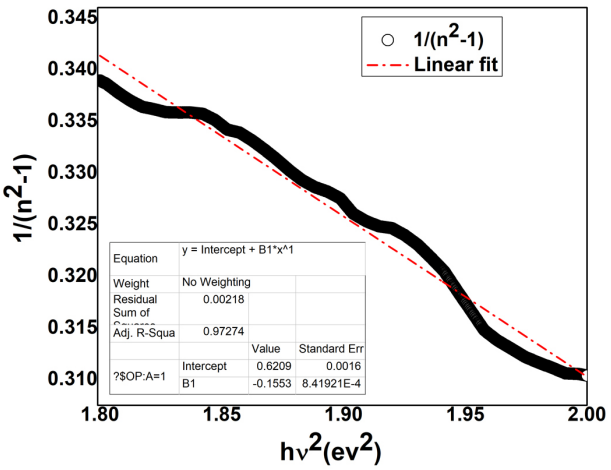


**Fig. 11** The curve of $1/(n^2–1)$ against $(hv)^2$ of SnS film. The intercept and slope are 0.62 and –0.15, respectively

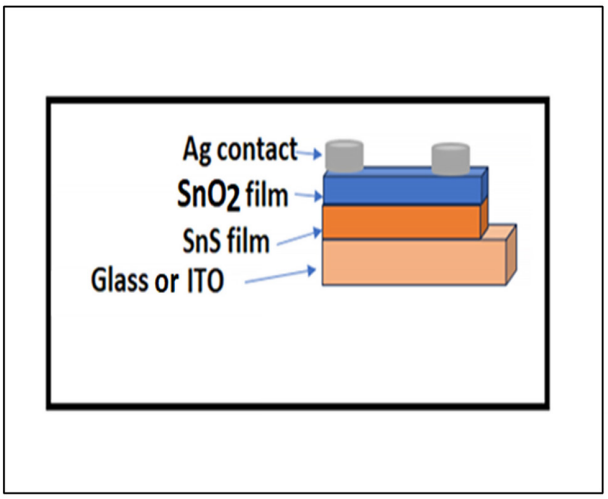


**Fig. 12** A schematic cross-section of the Ag/$SnO_2$/SnS/glass and Ag/$SnO_2$/SnS/ITO junction diodes

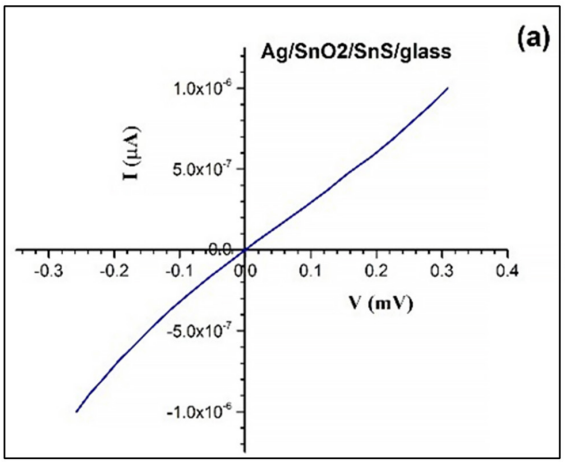


(a)

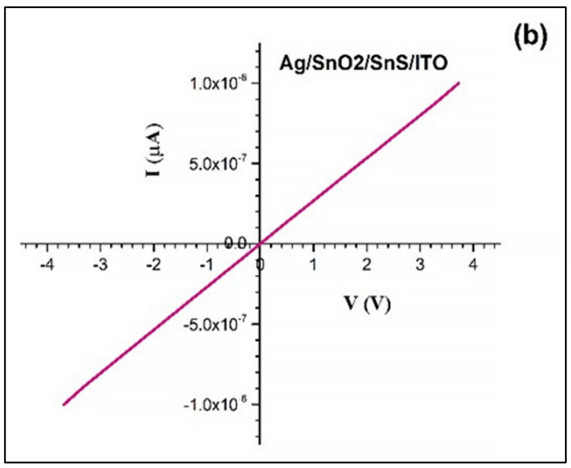


(b)

**Fig. 13** *I–V* characteristics of $SnO_2$/SnS/glass (a) and $SnO_2$/SnS/ITO (b) junctions

voltage range, respectively, for both junction onto glass and ITO substrates. Ag contacts based on films and substrates have an ohmic character, and the interface provides

no potential barriers to charge carriers. The current – voltage (*I–V*) characteristics of solar cell under light $SnO_2$/SnS/glass and $SnO_2$/SnS/ITO are studied as shown in Fig. 14.

The findings show the electrical transport mechanism of our PN junctions where the current increases with voltage. A good rectification is shown and the absence of a reverse current (leakage current) are noted. The presence of a potential barrier formed by heterojunction is confirmed by the direct polarization. The saturation current

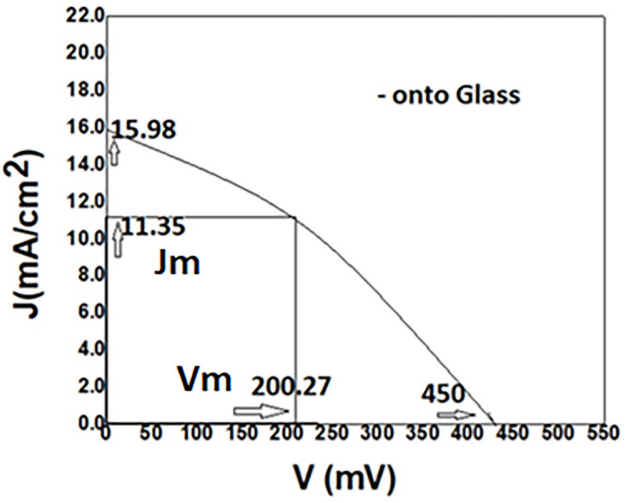


(a)

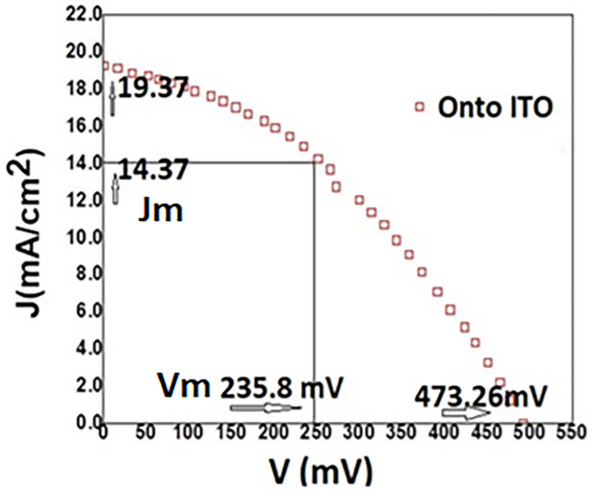


(b)

**Fig. 14** Photovoltaic parameters extraction of $SnO_2$/SnS/glass (a) and $SnO_2$/SnS/ITO (b) using approximative method of rectangle

$I_0$ is extracted from the graph *I–V* forward voltage side and the photovoltaic parameters like the short circuit current density ($J_{sc}$), open circuit voltage ($V_{oc}$), maximum current density ($J_m$), maximum voltage ($V_m$), fill factor (*FF*), efficiency ($\eta$) and saturation current ($I_0$) are listed in Table 3. The fabricated heterojunctions using *n*–SnS and *p–c*–Si demonstrated the reverse saturation current ($J_0$) of 1.7 μA as mentioned previously [37].

A transparent photovoltaic device built on thin films of *n*-Ga2O3/*p*-SnS heterojunction is reported [44]. The manufactured devices showed an optical transmittance of 70% and 50% in NIR and visible bands, respectively. The $Ga_2O_3$/SnS heterojunction quality was greatly enhanced by adjusting the film thickness of the thin-film $Ga_2O_3$, resulting in a high photocurrent density of 1.15 mA/cm$^2$ and an open-circuit voltage of 0.527 V. Under UV light exposure, such heterojunction power conversion efficiency was 2.9% [44].

In previous work, Al/ITO/i-ZnO/CdS/SnS/Mo/SLG is soda-lime glass, is fabricated by RF sputtering process by changing the working pressure from 0.6 Pa to 2.6 Pa as reported by Son et al. [35]. SnS film is used as absorber, while CdS is the buffer and ZnO is the window [35]. Under several pressures, the photovoltaic parameters are changed as: $V_{oc}$ is of 0.12–0.14 V, $J_{sc}$ is of 7.3–10.3 mA/cm$^2$, FF is of 35–39% and PCE is of 0.32–0.58% [35].

$TiO_2$/SnS/Ag solar cells are fabricated by spin coating route and heated within 25–85 °C. The $V_{oc}$, $J_{sc}$, *FF* and *PCE* parameters are found to be 0.33–0.42 V, 1.92–2.21 J/cm$^2$, 0.46–0.52 and 0.29–0.47% as a result of temperature for $TiO_2$/SnS/Ag junction as mentioned earlier [45]. The effect of Cu doping on the properties of the sprayed SnS films was reported [36].

The values of $I_{sc}$ and $V_{oc}$ are taken directly from the image, while the values of $I_m$ and $V_m$ are represented by a large rectangle drawn in the direction of the characteristic *I–V* [46–47], as shown in Fig. 14. The extracted curve parameters are used to calculate *FF* [46–47] according to,

$$FF = \frac{I_m V_m}{I_{sc} V_{oc}}. \tag{15}$$

**Table 3** Photovoltaic parameters of $SnO_2$/SnS/glass and $SnO_2$/SnS/ITO junctions

| | $J_{sc}$ (mA/cm$^2$) | $V_{oc}$ (mV) | $J_m$ (mA/cm$^2$) | $V_m$ (mV) | *FF* (%) | $\eta$ (%) | $I_0$ (nA) |
|---|---|---|---|---|---|---|---|
| $SnO_2$/SnS/glass | 15.98 | 450 | 11.35 | 200.27 | 0.32 | 2.27 | 10 |
| $SnO_2$/SnS/ITO | 19.37 | 473.26 | 14.37 | 235.84 | 0.37 | 3.38 | 1 |

$J_m$ and $V_m$ are marked in figure 14 a and b in annexe file values are comprised between 0.32 and 0.37, respectively, for our junction based SnS film on glass and ITO substrate as indicated in Table 3. Efficiency in terms of $V_{oc}$ and $FF$ is given as follows [46–47],

$$\eta = \frac{V_{oc} I_{sc} FF}{P_{in}}, \tag{16}$$

where $P_{in}$ is the light power per surface unity (1000 mW/cm$^2$). As confirmed by findings, the best efficiency is obtained for $SnO_2$/SnS/ITO which shows that junction deposited onto ITO substrate delivers an open circuit voltage of 473 mV and a short circuit current of 19 mA/cm$^2$ and fill factor of 0.369. It is reported that Al/$SnO_2$/n-Si/Au exhibited $I_0$ of 100 nA. Besides, a junction based on SnS film exhibits photovoltaic parameters such as $J_{sc}$ and $PCE$ 17.13 mA/cm$^2$ and 5.24%, respectively, as reported by Nguyen [13].

As reported earlier, under AM1.5 spectrum with light of 100 mW/cm$^2$ conditions, ITO/ZnO/CdS/SnS/Ag and ITO/ZnO/Cd(S,O)/SnS/Ag diodes are fabricated via RF sputtering route and exhibit, respectively, 0.22 V, 9.52 mA/cm$^2$, 0.26, and 0.55% and 0.28 V, 11.74 mA/cm$^2$, 0.34, and 1.12% [48]. Light and dark $I$–$V$ characteristics of the as-grown SnS thin film photodetectors are previously investigated. The current is increases by light exposure and reaches microamperes as cited earlier [26]. It is noticed that the photovoltaic parameters of FTO/CdS/$p$-SnS/C solar cells are 354 mV, 1.16 mA/cm$^2$, 0.32 and 0.13% [30]. The as-deposited $p$-SnS films fabricated at various pH values present the electrical conductivity values in light of 110 pS/cm and of 53 nS/cm and high photoresponse is found to be 17.4 [30].

## 4 Conclusion

This study focuses on SnS film and related junction fabricated by low-cost spray pyrolysis method. The results obtained allowed us to determine that the SnS films deposited by spray pyrolysis route have a cubic crystalline structure according to the plan (111) as confirmed by the X-ray diffractogram.

The optical measurements reveal a high transmittance of SnS within Vis-IR ranges with an optical band gap of 1.9 eV. The absorbance of SnS film is strong in UV giving 740 meV as Urbach energy.

Based upon SEM, AFM and TEM microscopic analyses, the SnS thin film exhibit a nano-flower feature with an average size of 200 nm.

The creation of surface leaflets in the films examined by SEM and AFM reveals a homogeneous, compact, and dense appearance. The various properties of heterojunctions based on $SnO_2$ and SnS deposited on glass and ITO substrates with SP deposit process are demonstrated and discussed. The current – tension characteristics of $SnO_2$/SnS/glass and $SnO_2$/SnS/ITO solar cells produce a good solar yield with good photovoltaic parameters when compared to other solar cells made of different materials.

## Acknowledgment

The research is included in the PRFU project under contract number N° B00L02UN310220220001 Oran University of sciences and technology USTO-MB.

Everyone reading this article is praying for my Parents' mercy. First author is grateful to staff of Department of Physics, Khadir Mohideen College, Adirampattinam for their help.

## References

[1] Ristov, M., Sinadinovski, G. J., Grozdanov, I., Mitreski, M. "Chemical deposition of TIN(II) sulphide thin films", Thin Solid Films, 173, pp. 53–58, 1989. https://doi.org/10.1016/0040-6090(89)90536-1

[2] Salwa, A. S., Salem, A. "Linear and nonlinear optical properties of SnS thermally evaporated thin films", Optik, 196, 163140, 2019. https://doi.org/10.1016/j.ijleo.2019.163140

[3] Brent, J. R., Lewis, D. J., Lorenz, T., Lewis, E. A., Savjani, N., Haigh, S. J., Seifert, G., Derby, B., O'Brien, P. "Tin(II) Sulfide (SnS) nanosheets by liquid-phase exfoliation of herzenbergite: IV–VI main group two-dimensional atomic crystals", Journal of the American Chemical Society, 137(39), pp. 12689–12696, 2015. https://doi.org/10.1021/jacs.5b08236

[4] Moon D. G., Rehan, S. , Yeon, D. H., Lee, S. M., Park, S. J., Ahn, S., Cho, Y. S. "A review on binary metal sulfide heterojunction solar cells", Solar Energy Materials Solar Cells, 200, 109963, 2019. https://doi.org/10.1016/j.solmat.2019.109963

[5] Olgar, M. A., Çiris, A., Tomakin, M., Zan, R., "Impact of in/ex situ annealing and reaction temperature on structural, optical and electrical properties of SnS thin films", Journal of Molecular Structure, 1241, 130631, 2021. https://doi.org/10.1016/j.molstruc.2021.130631

[6] Balakarthikeyan, R., Santhanam, A., Khan, A., El-Toni, A. M., Ansari, A. A., Imran A., Shkir, M., AlFaify, S. "Performance analysis of SnS thin films fabricated using thermal evaporation technique for photodetector applications", Optik, 244, 167460, 2021. https://doi.org/10.1016/j.ijleo.2021.167460

[7] Nouri, Y., Hartiti, B., Labrim, H., Ziti, A., Belfhaili, A., Batan, A., Fadili, S., Tahri, M., Thévenin, P. "Synthesis of tin monosulfide SnS thin films via spray pyrolysis method based on Taguchi design for solar absorber", Optical Materials, 131, 112669, 2022. https://doi.org/10.1016/j.optmat.2022.112669

[8] Jeganath, K., Choudhari, N. J., Pai, G. S., Rao, A., Raviprakash, Y. "Role of substrate temperature on spray pyrolysed metastable π-SnS thin films", Materials Science in Semiconductor Processing, 113, 105050, 2020.
https://doi.org/10.1016/j.mssp.2020.105050

[9] Kumar, P., Rao, G. K. "Synthesis and characterization of sulfate precursor based SnS thin films using SILAR technique at elevated solution temperature", Materials Today Communications, 35, 106194, 2023.
https://doi.org/10.1016/j.mtcomm.2023.106194

[10] Tian, H., Fan, C., Liu, G., Yuan, S., Zhang, Y., Wang, M., Li, E. "Ultrafast broadband photodetector based on SnS synthesized by hydrothermal method", Applied Surface Science, 487, pp. 1043–1048, 2019.
https://doi.org/10.1016/j.apsusc.2019.05.175

[11] Mohan V. V., Akshaya, K. C., Vijayakumar K. P. "Fabrication of p-type and n-type SnS thin films through vacuum-free deposition techniques", Materials Today Proceedings, 2023.
https://doi.org/10.1016/j.matpr.2023.02.104

[12] Sharma, D., Yadav, J., Mehta, B. R. "Reduced graphene oxide layer on nanostructured SnS thin films for improved visible light photoelectrochemical activity", Renewable Energy, 169, pp. 414–424, 2021.
https://doi.org/10.1016/j.renene.2021.01.010

[13] Nguyen, T. D., Dang, V. T., Hung, N. M., Arepalli, V. K., Kim, J., Raj, M., Nguyen, T. T. O. "Synthesis of Ag-embedded SnS films by the RF method for photovoltaic applications", Surfaces and Interfaces, 25, 101151, 2021.
https://doi.org/10.1016/j.surfin.2021.101151

[14] Aparna, N., Philip, R. S., Mathew, M. "Deposition of SnS thin films on various substrates at room temperature", Applied Surface Science Advances 18, 100510, 2023.
https://doi.org/10.1016/j.apsadv.2023.100510

[15] Kim, J., Kim, J., Yoon, S., Kang, J.-Y., Jeon, C.-W., Jo, W. "Single phase formation of SnS competing with SnS2 and Sn2S3 for photovoltaic applications: Optoelectronic characteristics of thin-film surfaces and interfaces", Journal of Physical Chemistry C, 122(6), pp. 3523–3532, 2018.
https://doi.org/10.1021/acs.jpcc.8b00179

[16] Kumar, R., Kar, M. "Lattice strain induced magnetism in substituted nanocrystalline cobalt ferrite", Journal of Magnetism and Magnetic Materials, 416, pp. 335–341, 2016.
https://doi.org/10.1016/j.jmmm.2016.05.035

[17] Rao, C. N. R., Pisharody, K. P. R. "Transition metal sulfides", Progress in Solid State Chemistry, 10, pp. 207–270, 1976.
https://doi.org/10.1016/0079-6786(76)90009-1

[18] Chalapathi, U., Poornaprakash, B., Park, S.-H., "Growth and properties of cubic SnS films prepared by chemical bath deposition using EDTA as the complexing agent", Journal of Alloys Compounds, 689, pp. 938–944, 2016.
https://doi.org/10.1016/j.jallcom.2016.08.066

[19] Abutbul, R. E., Segev, E., Zeiri, L., Ezersky, V., Makov, G., Golan, Y. "Synthesis and properties of nanocrystalline π-SnS – a new cubic phase of tin sulphide", RSC Advances, 6(7), pp. 5848–5855, 2016.
http://doi.org/10.1039/C5RA23092F

[20] Agashe, C., Takwale, M. G., Marathe, B. R., Bhide, V. G. "Structural properties of SnO2: F films deposited by spray pyrolysis", Solar Energy Materials, 17(2), pp. 99–117, 1988.
https://doi.org/10.1016/0165-1633(88)90010-X

[21] Benhaliliba, M. "ZnO a multifunctional material: Physical properties, spectroscopic ellipsometry and surface examination", Optik, 241, 167197, 2021.
https://doi.org/10.1016/j.ijleo.2021.167197

[22] Skelton, J. M., Burton, L. A., Jackson, A. J., Oba, F., Parker, S. C., Walsh, A. "Lattice dynamics of the tin sulphides SnS2, SnS and Sn2S3: vibrational spectra and thermal transport", Physical Chemistry Chemical Physics, 19, pp. 12452–12465, 2017.
https://doi.org/10.1039/C7CP01680H

[23] Sirohi, K., Kumar, S., Singh, V., Chauhan, N. "Hydrothermal synthesis of Cd-doped SnO2 Nanostructures and their Structural, Morphological and Optical Properties", Materials Today: Proceedings, 21(4), pp. 1991–1998, 2020.
https://doi.org/10.1016/j.matpr.2020.01.316

[24] Tauc, J., Grigorovici, R., Vancu, A. "Optical properties and electronic structure of amorphous germanium", Physica Status Solidi B, 15(2), pp. 627–637, 1966.
https://doi.org/10.1002/pssb.19660150224

[25] Ribeiro, T. C., Oliveira, M. H., Magalhaes-Paniago, R., Ferlauto, A. S., "From thin films to shaped platelets: effects of temperature gradient on SnS synthesis", Thin Solid Films, 721, 138507, 2021.
https://doi.org/10.1016/j.tsf.2020.138507

[26] Alagarasan, D., Varadharajaperumal, S., Kumar, K. D. A., Naik, R., Umrao, S., Shkir, M., AIFaify, S., Ganesan, R. "Influence of nanostructured SnS thin films for visible light photo detection", Optical Materials, 121, 111489, 2021.
https://doi.org/10.1016/j.optmat.2021.111489

[27] Javed, A., Khan, N., Bashir, S., Ahmad, M., Bashir, M. "Thickness dependent structural, electrical and optical properties of cubic SnS thin films", Materials Chemistry and Physics, 246, 122831, 2020.
https://doi.org/10.1016/j.matchemphys.2020.122831

[28] Mani, P., Manikandan, K., Prince, J. J. "Influence of molar concentration on triethanolamine (TEA) added tin sulfide (SnS) thin films by SILAR method", Journal of Materials Science: Materials in Electronics, 27, pp. 9255–9264, 2016.
https://doi.org/10.1007/s10854-016-4963-x

[29] Whittles, T. J., Burton, L. A., Skelton, J. M., Walsh, A., Veal, T. D., Dhanak, V. R. "Band alignments, valence bands, and core levels in the tin sulfides SnS, SnS2, and Sn2S3: Experiment and theory", Chemistry of Materials, 28(11), pp. 3718–3726, 2016.
https://doi.org/10.1021/acs.chemmater.6b00397

[30] Rodrıguez-Guadarrama, L. A., Escorcia-Garcıa, J., Alonso-Lemus, I. L., Campos-Álvarez, J. "Synthesis of π-SnS thin films through chemical bath deposition: effects of pH, deposition time, and annealing temperature", Journal of Materials Science: Materials Electronics, 32, pp. 7464–7480, 2021.
https://doi.org/10.1007/s10854-021-05459-8

[31] Moholkar, A. V., Pawar, S. M., Rajpure, K. Y., Almari, S. N., Patil, P. S., Bhosale, C. H., "Solvent-dependent growth of sprayed FTO thin films with mat-like morphology", Solar Energy Materials and Solar Cells, 92(11), pp. 1439–1444, 2008.
https://doi.org/10.1016/j.solmat.2008.06.010

[32] Ninan, G. G., Kartha, C. S., Vijayakumar, K. P. "Spray pyrolysed SnS thin films in n and p type: Optimization of deposition process and characterization of samples", Journal of Analytical and Applied Pyrolysis, 120, pp. 121–125, 2016. https://doi.org/10.1016/j.jaap.2016.04.016

[33] Kafashan, H., Baboukani, A. R. "Electrochemically deposited nanostructured Cd-doped SnS thin films: Structural and optical characterizations", Ceramics International, 50(3), pp. 5717–5727, 2024. https://doi.org/10.1016/j.ceramint.2023.11.354

[34] Burton, L. A., Colombara, D., Abellon, R. D., Grozema, F. C., Peter, L. M., Savenije, T. J., Dennler, G., Walsh, A. "Synthesis, characterization, and electronic structure of single-crystal SnS, Sn2S3, and SnS2", Chemistry of Materials 25(24), pp. 4908–4916, 2013. https://doi.org/10.1021/cm403046m

[35] Son, S.-I., Shin, D., Son, Y. G., Son, C. S., Kim, D. R., Park, J. H., Kim, S., Hwang, D., Song, P. "Effect of working pressure on the properties of RF sputtered SnS thin films and photovoltaic performance of SnS-based solar cells", Journal of Alloys and Compounds, 831, 154626, 2020. https://doi.org/10.1016/j.jallcom.2020.154626

[36] Sarica, E. "Investigation of spray pyrolyzed cubic structured Cu doped SnS films", Phosphorus, Sulfur, and Silicon and the Related Elements, 196, pp. 1103–1108, 2021. https://doi.org/10.1080/10426507.2021.1986498

[37] Mohan, V. V., Akshaya, K. C., Vijayakumar, K. P. "Type conversion as well as bandgap tuning of sprayed SnS thin film and initial trials on heterojunction diodes", Materials Today Proceedings, 2023. https://doi.org/10.1016/j.matpr.2023.02.216

[38] El-Mahalawy, A. M., Abdou, M. M., Wassel, A. R. "Physical and optoelectronic characteristics of novel low-cost synthesized coumarin dye-based metal-free thin films for light sensing applications", Materials Science in Semiconductor Processing 137, 106225, 2022. https://doi.org/10.1016/j.mssp.2021.106225

[39] Arulanantham, A. M. S., Valanarasu, S., Jeyadheepan, K., Kathalingam, A., Kulandaisamy, I. "Effect of sulfur concentration on the properties of tin disulfide thin films by nebulizer spray pyrolysis technique", Journal of Materials Science: Materials in Electronics, 28, pp. 18675–18685, 2017. https://doi.org/10.1007/s10854-017-7817-2

[40] Benouis, C. E., Benhaliliba, M., Yakuphanoglu, F., Silver, A. T., Aida, M. S., Juarez, A. S. "Physical properties of ultrasonic sprayed nanosized indium doped SnO2 films", Synthetic Metals, 161(15–16), pp. 1509–1516, 2011. https://doi.org/10.1016/j.synthmet.2011.04.017

[41] Wemple, S. H. "Refractive-index behavior of amorphous semiconductors and glasses", Physical Review, B, 7(8), pp. 3767–3777, 1973. https://doi.org/10.1103/PhysRevB.7.3767

[42] Wemple, S. H., DiDomenico, M., "Behavior of the electronic dielectric constant in covalent and ionic materials", Physical Review B, 3, pp. 1338–1351, 1971. https://doi.org/10.1103/PhysRevB.3.1338

[43] Jakhar, A., Jamdagni, A., Bakshi, A., Verma, T., Shukla, V., Jain, P., Sinha, N., Arun P. "Refractive index of SnS thin nano-crystalline films", Solid State Communications, 168, pp. 31–35, 2013. https://doi.org/10.1016/j.ssc.2013.06.013

[44] Kumar, N., Farva, U., Patel, M., Cha, W.-S., Lee, J., Kim, J. "n-Ga2O3/p-SnS heterojunction thin-films based transparent photovoltaic device", Journal of Alloys and Compounds, 921, 166177, 2022. https://doi.org/10.1016/j.jallcom.2022.166177

[45] Cheraghizade, M., Jamali-Sheini, F. "Symmetric strain- and temperature-dependent optoelectronics performance of TiO2/SnS/Ag solar cells", Surfaces and Interfaces, 25, 101223, 2021. https://doi.org/10.1016/j.surfin.2021.101223

[46] Benhaliliba, M. "The photovoltaic properties of a good rectifying Al/n-ZnO/p-Si/AL Schottky diode used in solar cell", Journal of Fundamental and Applied Sciences, 9(1), pp. 605–617, 2017. http://doi.org/10.4314/jfas.v9i1.35

[47] Würfel, P. "Physics of solar cells: from principles to new concepts", WILEY-VCH Verlag GmbH and Co. KGaA (2005). ISBN 9783527618545 https://doi.org/10.1002/9783527618545

[48] Ballipinar, F. "Tin sulfide (SnS) thin-film solar cells deposited by organic chemical vapor sulfurization based on CdS and high transmittance Cd(S,O) n-type layers with the superstrate device structure", MRS Communications, 10, pp. 660–666, 2020. https://doi.org/10.1557/mrc.2020.78